POTENTIAL PREDICTABILITY OF THE MADDEN–JULIAN OSCILLATION

BY D. E. WALISER, K. M. LAU, W. STERN, AND C. JONES

Ensembles of twin-predictability experiments suggest that successful dynamical forecasts of the Madden-Julian oscillation may offer one avenue for bridging the gap between medium to long-range weather forecasting and short-term climate prediction.

Since its discovery by Madden and Julian (1971, 1972) over two decades ago, the Madden–Julian oscillation (MJO) has continued to be a topic of significant interest due to its complex nature (Madden and Julian 1994) and the wide range of phenomena with which it interacts. The onset and break activity of the Asian–Australian monsoon system is strongly influenced by the propagation and evolution of MJO events (e.g., Yasunari 1980; Lau and Chan 1986; Hendon and Liebmann 1990a,b). Apart from this significant local influence, there are also important downstream influences that arise from the MJO. For example, the development of persistent North Pacific circulation anomalies during Northern Hemisphere winter has been linked to the evolution and eastward progression of convective anomalies associated with MJO events (e.g., Weickmann 1983; Liebmann and Hartman 1984; Weickmann et al. 1985; Ferranti et al. 1990; Lau and Philips 1986; Higgins and Schubert 1996; Higgins and Mo 1997; Mo 2000). In fact, a link has been shown to exist between rainfall variability along the western United States, including extreme events, and the longitudinal position of MJO convective anomalies (Mo and Higgins 1998a,b; Jones 2000; Higgins et al. 2000; Whitaker and Weickmann 2001). In addition, MJO convective activity has been linked to Northern Hemisphere summertime precipitation variability over Mexico and South America as well as to wintertime circulation anomalies over the Pacific–South American sector (Nogues-Paegle and Mo 1997; Mo and Higgins 1998c; Jones and Schemm 2000; Paegle et al. 2000). Recently, studies have also shown that particular phases of the MJO are more favorable than others in regards to the development of tropical storms/hurricanes in both the Atlantic and Pacific sectors (Maloney and Hartmann 2000; Mo 2000; Higgins and Shi 2001). Finally, the passage of

AFFILIATIONS: WALISER—Institute for Terrestrial and Planetary Atmospheres, State University of New York at Stony Brook, Stony Brook, New York; LAU—Climate and Radiation Branch, NASA Goddard Space Flight Center, Greenbelt, Maryland; STERN—Geophysical Fluid Dynamics Laboratory, Princeton University, Princeton, New Jersey; JONES—Institute for Computational Earth System Science, University of California, Santa Barbara, Santa Barbara, California
CORRESPONDING AUTHOR: Dr. Duane E. Waliser, Institute for Terrestrial and Planetary Atmospheres, Endeavour Hall #205, State University of New York at Stony Brook, Stony Brook, NY 11794-5000
E-mail: duane.waliser@stonybrook.edu
DOI: 10.1175/BAMS-84-1-33

In final form 8 August 2002

MJO events over the western Pacific Ocean has been found to significantly modify the thermocline structure in the equatorial eastern Pacific Ocean via their connection to westerly wind bursts (e.g., McPhaden and Taft 1988; Kessler et al. 1995; Hendon et al. 1998). This latter interaction has even been suggested to play an important role in triggering variations in El Niño–Southern Oscillation (ENSO; e.g., Lau and Chan 1988; Weickmann 1991; McPhaden 1999; Kessler and Kleeman 2000).

As influential as the MJO is on our weather and climate, a fundamental question yet to be adequately addressed concerns its theoretical limit of predictability. For example, it is well known that useful skill associated with deterministic prediction of most "weather" phenomena is limited to about 6–10 days (e.g., Thompson 1957; Lorenz 1965, 1982; Palmer 1993; Van den Dool 1994). Similarly, it has been found that the likely limit of predictability for ENSO is on the order of 12–18 months (e.g., Cane et al. 1986; Graham and Barnett 1995; Kirtman et al. 1997; Barnston et al. 1994, 1999). However, it is still yet to be determined what the corresponding metric is for the MJO phenomenon. The somewhat well-behaved nature of the MJO (e.g., equatorially trapped, preference for warm SSTs, seasonality) along with its intraseasonal timescales suggests that useful predictive skill might exist out to at least 15–25 days and maybe longer. Support for this suggestion comes from statistical predictive models of the MJO, which indicate useful skill out to at least 15–20 days lead time (e.g., Waliser et al. 1999a; Lo and Hendon 2000; Wheeler and Weickmann 2001; Mo 2001). However, as with any statistical model, these models are limited in the totality of the weather/climate system they can predict, their ability to adapt to arbitrary conditions, and their ability to take advantage of known physical constraints.

While there have been a number of predictive skill studies of the MJO (i.e., comparing forecasts to observations), these studies typically were performed with forecast models that exhibited rather poor simulations of the MJO. For example, the studies by Chen and Alpert (1990), Lau and Chang (1992), Jones et al. (2000), and Hendon et al. (2000) were all performed on the most recent or previous versions of the National Centers for Environmental Prediction (NCEP) Medium-Range Forecast (MRF) model's Dynamic Extended Range Forecasts (DERFs). In general these studies showed useful skill out to about 7–10 days. However, these skill limits are likely to be significant underestimates of the potential predictability due to the very weak MJO signature in the model. Moreover, since these studies were really measuring forecast skill of the model, their skill versus lead-time estimates are additionally hampered by the difference in phase speeds between the model and observations and the influence from poorly known/specified initial conditions. Thus, ascertaining even a gross estimate of the limit of predictability for the MJO from these studies is neither appropriate nor feasible.

In this study, we determine an estimate for the theoretical limit of dynamic predictability of the MJO by conducting a set of twin numerical predictability experiments (e.g., Thompson 1957; Lorenz 1965; Charney et al. 1966; Shukla 1985) with a given model—one that has a reasonable representation of the MJO's space–time variability. Using this methodology, we attempt to address the following two questions. What is the typical limit of useful predictability for the tropical MJO phenomenon? How is this limit influenced by the phase or strength of the MJO (e.g., convection over the Indian versus the western Pacific Oceans)? Our study focuses on the Northern Hemisphere winter and thus the archetypal equatorial-propagating MJO phenomena. A separate study (Waliser et al. 2002, manuscript submitted to *Quart. J. Roy. Meteor Soc.*) addresses the limit of predictability of the Northern Hemisphere summer (northeastward propagating) mode of intraseasonal variability (e.g., Wang and Rui 1990; Wang and Xie 1997), and the implications this limit has on Asian summer monsoon predictions.

The next section describes the model employed for this study, and that is followed by a section describing the experimental framework and the analysis methods. The section titled "Results" presents the results of the experiments. The last section presents a summary of the results, considers the caveats of the model and analysis, and discusses the implications of this result with regards to the predictability of other weather/climate phenomena that are influenced by the MJO.

MODEL. The model used in these experiments is the National Aeronautics and Space Administration (NASA) Goddard Laboratory for the Atmospheres (GLA) general circulation model (GCM). This model was derived from earlier version described by Kalnay et al. (1983). Modifications have included increased vertical resolution and several changes in the parameterizations of radiation, convection, cloud formation, precipitation, vertical diffusion, and surface processes (Sud and Walker 1992; Phillips 1996). The horizontal representation uses surface finite differences on a $4° \times 5°$ (latitude × longitude) energy and momentum conserving A grid (Arakawa and Lamb 1977). The horizontal advection of the atmospheric variables is

accurate to the fourth order (Kalnay et al. 1983). The vertical domain has 17 unequally spaced sigma levels extending from the surface to about 12 hPa. At every dynamical time step, a 16-order Shapiro (1970) filter (with a timescale of 90 min) is applied to the prognostic fields; a Fourier filter is also used in polar latitudes. Negative moisture values are filled by "borrowing" moisture from the level below, and from neighboring horizontal grid boxes at the lowest vertical level. Horizontal diffusion is not included and the effects of vertical diffusion are treated by the level-2½ second-order turbulence closure model of Helfand and Labraga (1988).

Near the surface, the planetary boundary layer is treated as an extended surface layer with a viscous sublayer in the space between the surface and the tops of the surface roughness elements. Appropriate parameterizations are utilized to determine turbulent fluxes in the different planetary boundary layer (PBL) subregions. Both seasonal and diurnal cycles in the solar forcing are simulated with the atmospheric radiation treatment of Harshvardhan et al. (1987). The formulation of the convection follows the scheme of Arakawa and Schubert (1974), as implemented in discrete form by Lord and Arakawa (1980). The model orography is based on the 1° × 1° topographic height data of Gates and Nelson (1975), which has been area averaged over the 40 × 50 grid boxes. The resulting orography is smoothed using a 16th-order Shapiro (1970) filter, and a Fourier filter poleward to 60° latitude. Negative terrain heights resulting from the smoothering process are set to zero. Land surface processes are simulated as in the Xue et al. (1991) modification of the model of Sellers et al. (1986).

In general, the GLA model performed very well with respect to its representation of the MJO in the Slingo et al. (1996) Atmospheric Model Intercomparison Project (AMIP) study. It, along with two other models [the United Kingdom Met Office (UKMO) model and version 2 of the Community Climate Model (CCM2)], exhibited variability closely resembling the observed features of the oscillation. In fact, a more rigorous comparison of the MJO in the GLA and UKMO models by Sperber et al. (1996) showed that of the two models, the GLA model tended to produce a better representation of the eastward propagation of convection and its associated cyclonic and anticyclonic circulation anomalies. While modest improvements in the GLA simulation of the MJO were obtained by incorporating a weakly coupled SST feedback (Waliser et al. 1999b), this study utilizes the fixed SST version of the model. A future study will report on the influences of SST coupling and interannual SST anomalies on the predictability of individual MJO events.

EXPERIMENTAL FRAMEWORK. As a basis for selecting initial conditions for a number of MJO events, a 10-yr simulation using climatological SSTs was performed and daily averages (four 6-h values) of a number of fields were saved. From this simulation, MJO events were chosen based on an extended empirical orthogonal function analysis (EEOF) of rainfall data from the region 32°N–32°S and 32.5°E–92.5°W. This region tends to encompass most of the variability in rainfall that is associated with the MJO (e.g., Lau and Chan 1986; Wang and Rui 1990). To isolate the intraseasonal timescale, and thus the MJO, the data were first bandpassed with a 30–90-day Lanczos filter (Duchon 1979). EEOF analysis, using temporal lags from –7 to +7 pentads, was then performed on pentad averages from Northern Hemisphere "wintertime," hereafter defined as November–April. The spatial–temporal pattern for the first EEOF mode, shown in Fig. 1, depicts the bulk characteristics of the typical cycle of the model MJO in terms of rainfall. The spatial–temporal pattern of mode 2 (not shown) exhibits a quadrature relation with mode 1; otherwise the two modes are very similar. The first (second) mode contains 6.0% (5.9%) of the variance of the time-lagged sequences of the bandpassed data. These percentages are similar to those that would be obtained for the first two modes using a conventional, nonlagged EOF approach (i.e., 6.5% and 5.9%, respectively).

To illustrate the degree of realism associated with the model's MJO, the same EEOF analysis was performed on 10 yr (1988–98) of pentad rainfall data from Xie and Arkin (1997). The first EEOF mode (not shown) from this analysis has a very similar structure to the model EEOF mode shown in Fig. 1, although the observed mode captures more variance (8.3%). Composite MJO events from the model and observations were constructed by averaging the bandpassed rainfall and VP200 data for all pentads that had an EEOF mode-1 time series amplitude greater than 0.8. For the model (observations), this included 19 (14) pentads. This resulted in a composite MJO, in terms of rainfall and VP200, extending from lags –7 pentads to +7 pentads (similar in structure to Fig. 1). To compactly illustrate the model–data comparison, lags –7 and –6 were averaged together (to be referred to as lag –6.5), lags –5 and –4 pentads were averaged together (to be referred to as lag –4.5), and so forth, giving composite maps separated by two pentads (i.e., 10 days). The composite maps for lags –4.5, –2.5, –0.5,

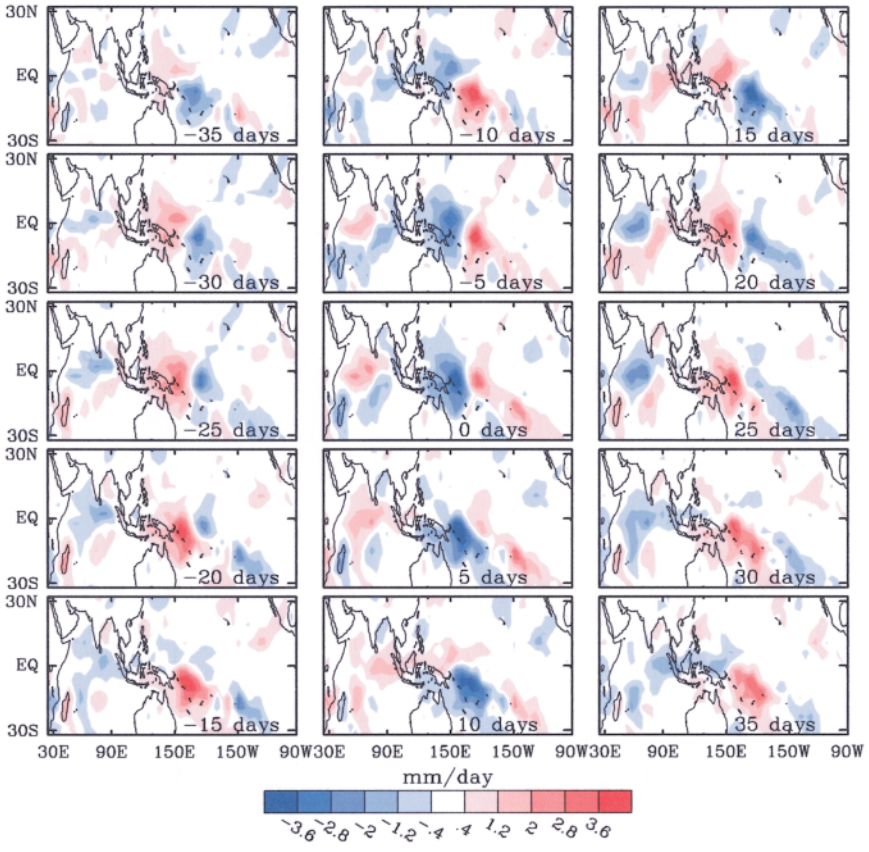

Fig. 1. First mode EEOF of filtered (30–90 days) NH winter (Nov–Apr) model rainfall for the tropical domain in 32°N–32°S and 32.5°E–92.5°W. Time lags extend from –35 days (i.e., –7 pentads) in the upper-left corner to +35 days (i.e., +7 pentads) in the lower-right corner. See section titled "Experimental framework" for details.

+1.5, and 3.5 pentads for both the observed and model MJO composites are shown in Fig. 2. A comparison of these two life cycles shows that the model MJO has fairly realistic characteristics in terms of the space–time variability of MJO-induced rainfall and VP200. This includes the overall timescale, the magnitude and locations of the variability, the propagation speed, etc. One of the more significant shortcomings in the model for this study, however, is its weaker rainfall variability exhibited in the eastern Indian Ocean and southern Maritime Continent region (cf. Waliser et al. 2001), a characteristic that is quite common in AGCMs' representations of intraseasonal variability (Waliser et al. 2002, manuscript submitted to *Climate Dyn.*). The potential implications associated with this shortcoming for this study are discussed in the summary.

Candidate MJO events to use for initial conditions were chosen from the amplitude time series associated with model EEOF modes 1 and 2; these time series are shown in Fig. 3. Given that these modes capture the propagating nature of the MJO, selecting periods when the amplitude of these time series is large will tend to capture strong, propagating MJO events. For the purpose of selecting specific days for initial conditions, these two pentad time series were interpolated to daily values. The two series have maximum correlation (0.95) at a lag of +/– ~ 12 days, indicating a dominant period of about 50 days. This is consistent with the discussion above regarding the quadrature relation of the first two EEOF modes. Note that when the mode-1 time series is positive (negative), rainfall tends to be high in the western Indian (western Pacific) Ocean, and when the mode-2 time series is positive (negative), rainfall tends to be high in the eastern Indian (central Pacific Ocean/South Pacific convergence zone) Ocean. Thus, by selecting periods of both positive and negative values of these two series, four separate "phases" of the MJO can be distinguished based on the longitudinal position of the heating. For each of these four phases, the 15 events with the greatest amplitudes for each of the four phases were selected.[1] These events are highlighted in Fig. 3.

In order to contrast the difference in atmospheric predictability between periods of high MJO activity to those with little or no MJO activity, 15 initial conditions were also chosen from periods in which neither of the above modes, nor their Northern Hemisphere (NH) "summertime" (May–October) counterpart, were strongly exhibited in the model atmosphere. The selection was performed as follows. The amplitude time series for EEOF modes 1–4 for

[1] In cases in which the occurrence was too close to the beginning or end of the 10-yr record preventing subsequent analysis (e.g., bandpassing, 90-day integration), the event(s) with the next largest amplitude(s) were selected.

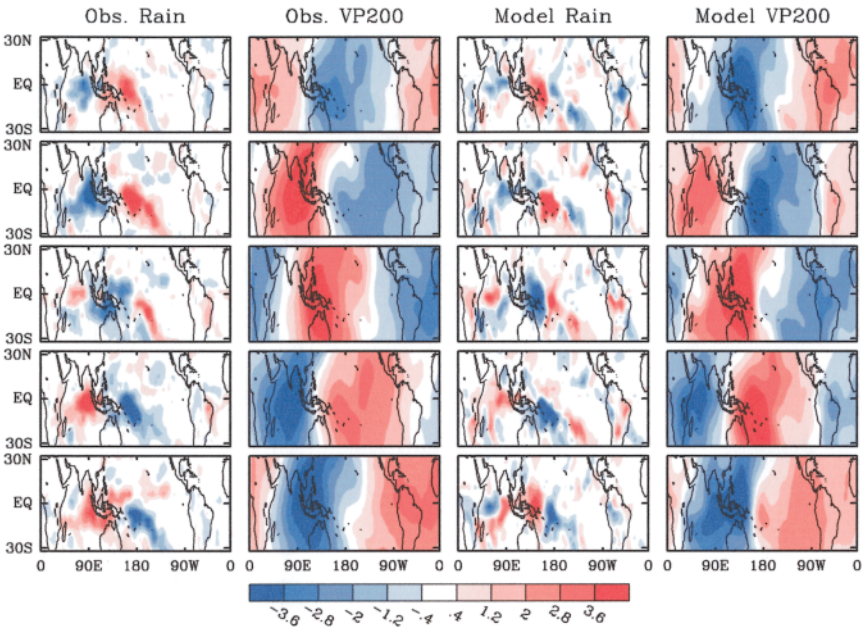

FIG. 2. Composite NH winter (Nov–Apr) MJO from observations (left columns) and the model (right columns). Sequential maps are separated by 10 days. Units for rainfall (200-hPa velocity potential) are mm day^{-1} (10^6 × m^2 s^{-1}). See section titled "Experimental framework" for a description of their construction.

the Northern Hemisphere winter, along with the analogous four series for the summer, were squared, added together, and then smoothed with a 51-day (~ MJO cycle) running filter. This combined series, shown in Fig. 3 (bottom), gives a bulk index of generalized intraseasonal activity. The 15 events with the lowest values of this index were selected to represent low MJO activity conditions with the additional criteria that the events had to occur at least 10 days apart. The latter criterion was applied in order to get a sample of distinct atmospheric states of low MJO activity. Hereafter, these cases, shown as Xs in Fig. 3 (bottom), will be referred to as null events. Figures 4 and 5 show the composite rainfall and 200-hPa velocity potential (VP200), respectively, for the 15 initial conditions selected for each of the four MJO phases as well as the null events.

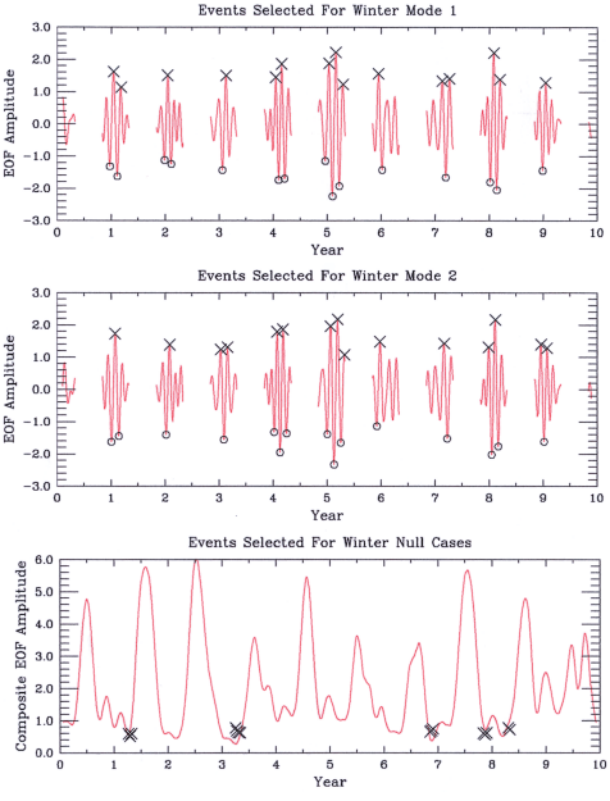

FIG. 3. Amplitude time series for the (top) first and (middle) second EEOF of filtered (30–90 days) NH winter model rainfall. (top) and (middle) The Xs and Os represent the time periods selected for MJO-event initial conditions. (bottom) Composite EEOF amplitude time series representing generalized intraseasonal activity. The 15 Xs in this panel represent the time periods selected to represent little or no MJO activity (i.e., the null events). The minimum spacing between the Xs in this panel is 10 days and all Xs occur in NH winter (Oct–Apr). See section titled "Experimental framework" for details.

Two perturbations were performed for the 75 cases selected [(4 MJO phases + null phase) × 15 events]. The perturbation initial conditions were determined in a fairly simplistic manner. Given the day of the month that the initial condition occurs, day-to-day root-mean-square (rms) differences were computed (on the model's sigma surfaces) from the daily averaged values of the model's four prognostic variables (u,v,T,q) for that particular month. This process was meant to provide some spatial structure to the perturbation, whereby larger day-to-day variability would translate into more uncertainty in the initial conditions. These rms values were then multiplied by a random number scaled between –0.1 and 0.1 for the first set of perturbations and –0.2 and 0.2 for the second set. These "errors" were then added to the original ini-

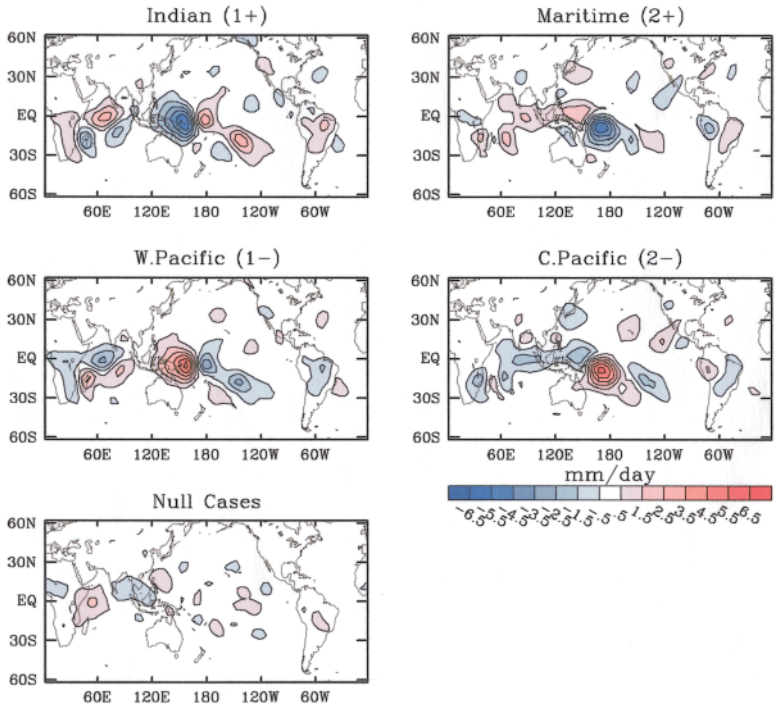

FIG. 4. Composite filtered (30–90 days) rainfall anomalies for the 15 initial conditions selected to represent the four "phases" of the MJO (upper four panels) as well as the null cases (lower panel). For example, the upper-left panel [i.e. Indian (1+)] is the average rainfall anomaly from the 15 initial conditions indicated by the Xs in the upper panel (i.e., mode 1) of Fig. 3. Similarly, for the other panels. Except in the null case (lower left), the headings indicate the geographic region of the most intense MJO-related rainfall (i.e., Indian Ocean for the upper left) as well as the rainfall EEOF mode and sign (e.g., 1+ indicates EEOF mode 1 > 0).

tial condition's prognostic values to produce an alternative initial condition. The different size error between the first set and second set will be used to provide some information on the sensitivity of the predictability to the size of the initial condition perturbation.

For each alternative initial condition, the model was integrated for 90 days. To isolate the MJO phenomena and distinguish its predictability from high-frequency weather fluctuations, the 120 days of model simulation prior to the initial condition were combined with the 90-day "forecasts" and the result bandpassed filter during the same 30–90-day filter described above. A triangular taper 40 days long was applied at either end of these 210-day series. To illustrate the sensitivity of the results to the use of such a filter, specifically its "edge" effects, results will also be shown for persistence forecasts as well as the case of using 10-day-average data.

RESULTS. While there are a number of ways to define predictability for atmospheric phenomena (e.g., Shukla 1985; Stern and Miyakoda 1995; Anderson and Stern 1996; Yang et al. 1998; Schneider and Griffies 1999), the approach taken here attempts to make a relatively conservative estimate of the limit of useful predictability for the MJO. When the MJO is active, it tends to exhibit an oscillatory form in which the amplitude of the oscillation can be said to represent a measure of the "signal." Of interest here is how long before the forecast errors resulting from the imprecise initial conditions grow to be as large as this signal. Schematically, this is illustrated in Fig. 6, where the solid thick line represents the control simulation and the two solid thin lines represent the perturbed cases. Thus for the MJO (or null) events selected, we will examine how the mean forecast error compares to the mean signal (e.g., Kleeman and Moore 1999). The signal for a given MJO event is defined as the variance within a sliding window that is large enough to encompass the entire event (~50 days):

$$\sigma^2_{S_{ij}} = \frac{1}{2L+1}\sum_{\tau=-L}^{L} X^{0^2}_{i,j+\tau}\,. \qquad (1)$$

The forecast error for a given event is defined as the mean-square difference between the perturbed case and the control case

$$\sigma^2_{E_{ijk}} = (X^k_{ij} - X^0_{ij})^2. \qquad (2)$$

In the above equations, X is the geophysical quantity being analyzed (e.g., VP200), i is the MJO event, j is the day number relative to the initial forecast date, and k is the perturbation number with X^0 representing the control case. The mean signal and mean-square forecast error for a given set of events are then simply defined as

$$\overline{\sigma^2_{Sj}} = \frac{1}{N}\sum_{i=1}^{N}\sigma^2_{S_{ij}} \qquad (3)$$

$$\overline{\sigma^2_{Ej}} = \frac{1}{2N}\sum_{k=1}^{2}\sum_{i=1}^{N}\sigma^2_{Eijk}. \qquad (4)$$

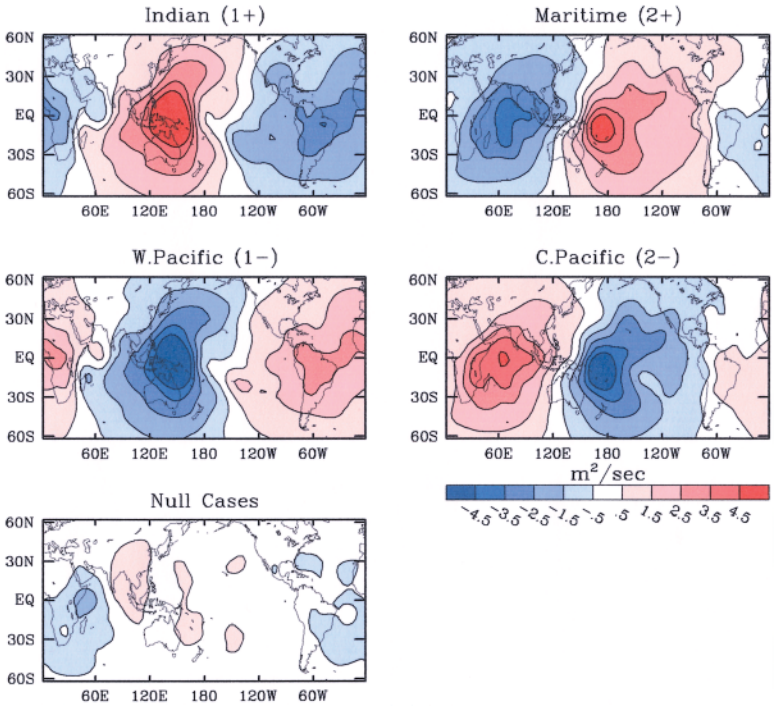

FIG. 5. Same as Fig. 4, except for 200-hPa velocity potential.

In the above equations, N is typically set to 15 (e.g., 15 events for a particular phase of the MJO) or 60 (all MJO events), L is set to 25, and X represents daily values of intraseasonally filtered data. Parameter settings of this sort, considered the standard or control, provide the means to diagnose the predictability of the model's MJO. However in some cases, X represents daily unfiltered data and L is set to 5. These latter calculations are for the purposes of diagnosing the predictability of the model's weather and comparing it to the predictability of the model's MJO (i.e., Fig. 12).

Given that the two sets of perturbations (k = 1,2) use different size perturbations, the error growth for these two sets can be calculated separately in Eq. (4) by averaging only over $k = 1$ in one case, and only over $k = 2$ in the second. Using the above definitions, a predictability ratio can be defined as

$$\overline{\sigma_{Sj}^2} / \overline{\sigma_{Ej}^2}, \qquad (5)$$

with the implication that at early lead times this ratio will be much larger than 1 and at the point it becomes of order 1, little useful predictability remains. Note that an alternative to the above approach would be to perform a much larger ensemble of forecasts for one or a few events and compare the ensemble spread at any given lead time to the size of the mean signal. This represents a more typical approach of comparing signal to "noise." However, given limited computing resources, this approach drastically reduces the number of events that can be represented in the analysis. For example, given the same number of simulations, only three events could be examined if the ensemble size was set to 10. Since it is unknown how variable the predictability of the MJO might be from one event to the next, selecting one or a few events to be representative might prove difficult. For this reason, we opted for the approach outlined above. In any case, to test the sensitivity of the results to the approach adopted, we also performed 90-day forecasts for a 15-member ensemble for a single MJO event [starting from 31 January, year 8; see X in Fig. 3 (top)]. The predictability characteristics for this ensemble were found to generally agree with those described below that were based on more events (i.e., 60) but with fewer members in each ensemble (i.e., 2) as outlined above.

Figure 7 illustrates the temporal evolution of VP200 for the selected events (i.e., N = 15 for each case; thin solid lines) for a region located in the western Pacific Ocean. For each panel, the solid thick lines represents the ensemble mean of the events chosen, the dotted thick lines depict the standard deviation associated with this ensemble, and the thin dotted lines represent the square root of the signal as defined

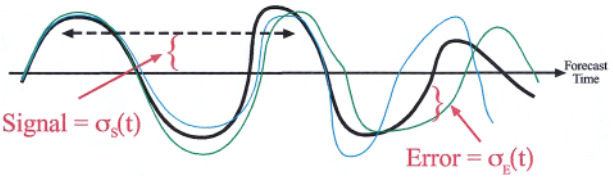

FIG. 6. Schematic depiction of the evolution of an MJO event vs forecast time for a control forecast (thick line) as well as two forecasts with perturbed initial conditions (thin lines). The forecast error at any given time [$\sigma_E(t)$] between the control forecast and a perturbed forecast is the difference between the two time series. The signal of the MJO event at any given time [$\sigma_s(t)$] is represented as the running variance (shown here in terms of std dev) of the time series, where the averaging length is long enough to encompass a typical MJO period. Thus the "signal" is a representation of the overall amplitude of a given MJO event. See Eqs. (1)–(4) and associated text in the section titled "Results."

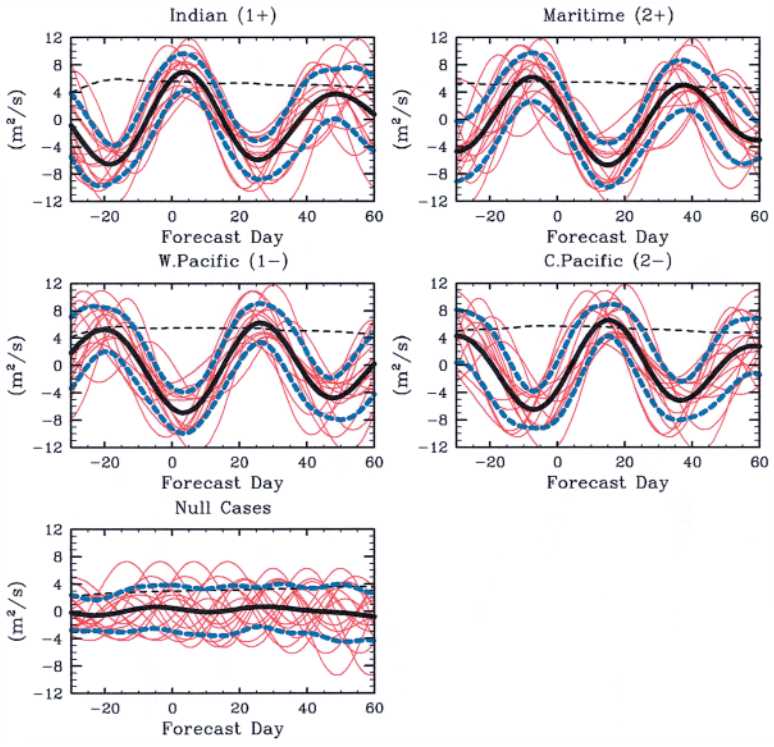

FIG. 7. The thin solid lines depict the evolution of filtered (30–90 day) 200-hPa velocity potential over the western Pacific Ocean (4°N–12°S, 147.5°–162.5°E) for the selected MJO events (upper four panels) and null cases (lower panel). Except in the null case (lower left), the headings indicate the geographic region of the most intense MJO-related rainfall at the start of the forecast as well as the rainfall EEOF mode and sign (see Fig. 4). The thick solid lines are the means of the 15 time series in each panel. The thick dashed lines are the mean values plus and minus one std dev. The thin dashed lines are the square root of the mean MJO signal as defined by Eq. (3). Forecast day 0 is the day that the forecasts will begin from perturbed initial conditions.

in Eq. (3). Note that forecast day "0" is the day that the forecasts will begin from perturbed initial conditions. The upper four panels illustrate the VP200 evolution for the events that were selected to represent four different phases of the MJO. The relatively good coherence in the temporal evolution between these events within each panel demonstrates that the MJO event selection procedure performed as intended. The lower panel illustrates the VP200 evolution for the events that were selected to represent cases with little or no MJO activity. In this case, the events show little coherence and also exhibit significantly weaker amplitudes.

Figure 8 shows the mean signal [thick solid blue; Eq. (3)] and mean-square forecast errors [thick solid black; Eq. (4)] versus lead time for VP200 for the selected events for the same western Pacific Ocean region. Ninety-five percent confidence limits on these mean values are also shown (thin dashed lines). In addition, mean-square forecast errors for persistence are also shown. For these persistence forecasts, the daily average value from the day of the initial conditions was persisted for 90 days. The data are then bandpassed in the same manner as the dynamical forecasts. It is worth noting the fact that the forecast errors are not zero at 0-days lead due to the use of the bandpass filter to isolate the MJO phenomena. The application of such a filter introduces useful information into the early forecast early period from the period prior to the forecast and erroneous information into period prior to the forecast from the forecast itself. For the most part, the mean signal remains relatively constant through the period shown. However, since the MJO (null) events were chosen based on maxima (minima) found in the EEOF amplitude time series, a slight decrease (increase) in the signal is exhibited away from forecast day 0 for the MJO (null) events. In addition, part of the decrease in the signal at long lead times (> ~ 45 days) is due to the application of the triangular taper before bandpassing (see the section titled "Experimental framework").

Of interest here is the forecast lead time when the mean forecast error and the mean signal tend to be equal. For this western Pacific Ocean region, this tends to occur at about 20–30 days. Comparing the upper four panels shows that this intersection of signal and forecast error occurs soonest (~ 20 days) when the convection is over the Maritime region at the start of the forecast and latest (~ 30 days) when the convection starts in the Indian or central Pacific Ocean. This difference might be related to the fact that longer-lead predictions of MJO variability for the western Pacific (or any region) are probably less skillful within the convective regime of the MJO. For the events when the convection starts in the Indian Ocean, the western Pacific first goes through a suppressed phase (see Fig. 7) during days 0–20, which is then followed by the development of the convective phase during days 20–30. Having the suppressed phase in the early part of the forecast appears to lend skill to the prediction and lengthen the period of use-

ful predictability. On the other hand, for the events when the convection starts over the Maritime region, the skill appears quite good in the first 10–15 days when evolving from suppressed to convective conditions. However, beyond this time the forecast skill degrades rapidly. It should be noted that the size of the confidence limits (black and blue dotted lines) suggests that the longitudinal dependencies of the predictability measures illustrated in Fig. 8 (as well as Figs. 11 and 12) should be considered with some caution.

Considering all the selected MJO events together (lower-left panel in Fig. 8) indicates that useful predictability extends to about 25–30 days. Note that the dynamical skill typically exceeds that associated with the persistence score by about 5–10 days. Due to the use of the bandpass filter to isolate the MJO, the persistence forecasts shown here essentially represents a crude empirical form of MJO forecasting (cf. Wheeler and Weickmann 2001). For the null cases (lower-right panel) useful predictability tends to exist for lead times less than about 15 days for this location. This appears to result from an error growth rate (at early lead times) that is not too dissimilar from the high-amplitude MJO cases in combination with a much weaker amplitude associated with the MJO signal. Thus the errors simply obtain the magnitude of the signal at a much earlier lead time. It is also worth pointing out that persistence appears to provide a more competitive forecast for the null events as compared to the MJO cases. This is not completely unexpected since for the null cases the atmosphere is in a more quiescent (i.e., persistent) state, in an intraseasonal sense, than for the cases when the MJO is strongly exhibited.

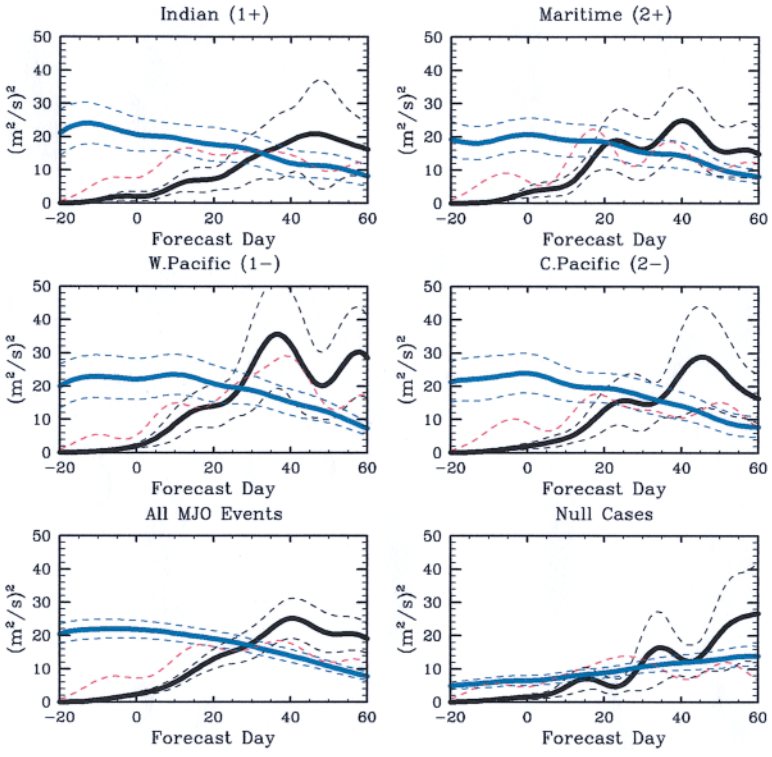

Fig. 8. The thick solid black and blue lines are the mean-squared forecast error [Eq. (4)] and mean MJO signal [Eq. (3)], respectively, for the filtered (30–90 day) 200-hPa velocity potential over the western Pacific Ocean (4°N–12°S, 147.5°–162.5°E) for the selected MJO events [upper four panels (*N* = 30) and lower left panel (*N* = 120)] and for the null cases [lower-right panel (*N* = 30)]. The thin dashed black and blue lines depict the 95% confidence limits for these means using a Student's *t* test. Except in the lower two panels, the headings indicate the geographic region of the most intense MJO-related rainfall at the start of the forecast as well as the rainfall EEOF mode and sign (see Fig. 4). The lower-left panel includes all MJO events (i.e., all the series in the upper four panels). The dotted red lines are the mean-squared forecast error for a persistence forecast (see section titled "Results"). Forecast day 0 is the day that the forecasts begin.

To illustrate the sensitivity of the forecast errors to the initial perturbation size, the top two panels in Fig. 9 shows the same information as the lower-left panel in Fig. 8, except that the left (right) panel contains the MJO forecasts that had a perturbation multiplier of 0.1 (0.2) (see section titled "Experimental framework"). Thus each of these panels is based on the same 60 MJO cases, but they differ in the size (and random nature) of the perturbation applied. As a reminder, the lower-left panel in Fig. 8 is composed of both these sets of forecasts (i.e., $N = 120$). The results illustrate some modest dependence on perturbation size, at least for the magnitude of the perturbations considered in this study. The mean-square forecast error for the forecasts with the smaller perturbation size (upper left) crosses the mean signal at 30 days, while for the forecasts with the larger perturbation size (upper right) this intersection occurs at 25 days. Although the qualitative aspect of this result is somewhat expected, the quantitative aspects should be considered with some caution given the confidence limits shown. The lower two panels in Fig. 9 demonstrate the influence of the use of the 30–90-day bandpass filter as a means of isolating the MJO. It contains the

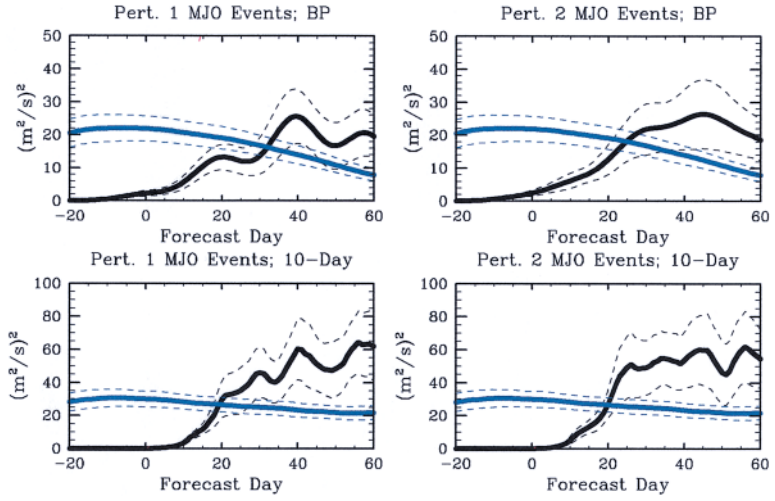

FIG. 9. (top) Same as lower-left panel of Fig. 8, except that the left (right) panel only contains the 60 out of the 120 forecasts having random perturbations to the initial conditions with a magnitude of 0.1 (0.2) times the daily rms values (see section titled "Experimental framework"). (bottom) Same as upper plots, except using 10-day running mean data rather than 30–90-day bandpass filtering.

same information as the upper two panels, except for the case of using a simple 10-day box average instead. Since less variability is filtered out in this case, the signal (thick blue line) is larger than for the use of the bandpass filter. Correspondingly, the error growth rate is somewhat larger. However, considering these two quantities together still suggests that useful predictability extends to about 20 days for the selected MJO events. As with the upper panels, there is some evidence for forecast errors in these two lower panels to be larger for the larger perturbation cases, at least in the 20–30-day range.

To illustrate the spatial dependence of the results discussed above, Fig. 10 shows the MJO signal [left panels; Eq. (3)] and mean-square forecast error [right panels; Eq. (4)] for VP200 at three lead times (5, 15, and 25 days) between 60°N and 60°S. As expected the large values for the MJO signal, and thus large values of the forecast error as well, are predominately confined to the tropical latitudes of the Eastern Hemisphere. At 15 days, the mean signal is still considerably larger than the mean forecast error for this entire region. Even out to 25 days in this region, the mean signal is still slightly larger than the mean forecast error indicating useful predictability at this lead time.

While VP200 is a useful indicator of tropical circulation patterns associated with the MJO, its relevance to weather and short-term climate variations at the surface is quite limited. As in most weather and climate forecasting contexts, rainfall is not only a highly relevant quantity to predict, it is also typically one of the most difficult. Figure 11 shows the same information presented in Fig. 10 but for rainfall instead of VP200. As expected the area exhibiting strong MJO variability is significantly reduced for rainfall as compared to VP200 (i.e., Figs. 4,5). Apparent is the expected reduction in predictability. For rainfall, the error at 15-day lead time is approaching the size of the signal. While 15 days

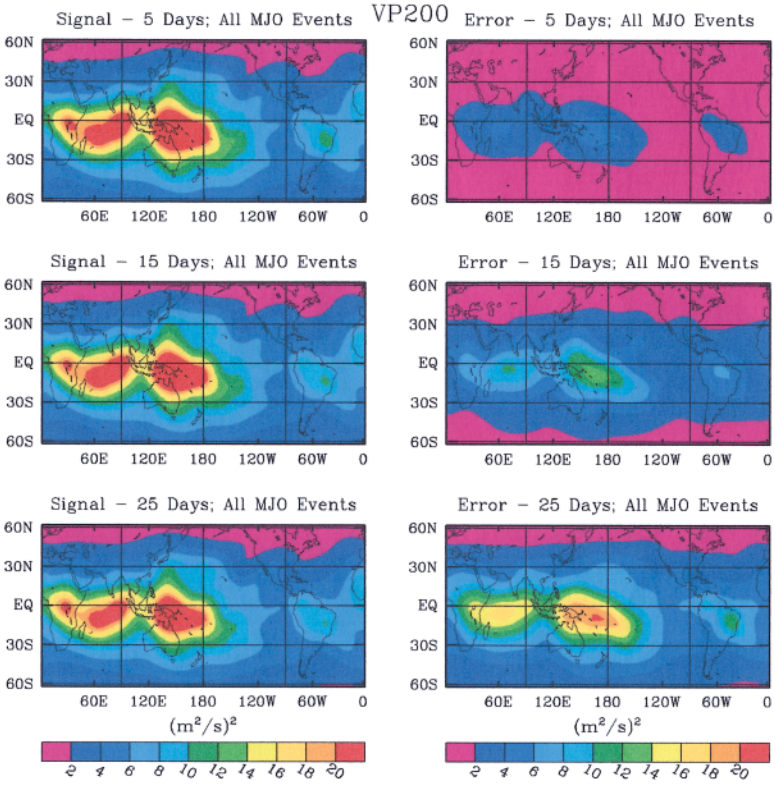

FIG. 10. (left) The MJO mean signal [see Eq. (3)] and (right) mean forecast error [see Eq. (4)] for all the selected events MJO events combined at lead times of (top) 5, (middle) 15, and (bottom) 25 days for filtered (30–90 days) 200-hPa velocity potential.

represents about a factor of 2 reduction relative to the lead times of useful predictability for VP200, taken in the context of typical weather variations, it still represents considerable utility.

To show more directly how the signal and error compare versus lead time, predictability ratios defined by Eq. (5) were computed for VP200, rainfall and 500-hPa geopotential heights (hereafter H500). As mentioned earlier, computations were done on bandpassed data with $L = 25$ (Eq. (1)] to diagnose the predictability of the model's MJO as well as on unfiltered daily data with $L = 5$ to diagnose the predictability of the model's weather. Figures 12a,b show domain-averaged predictability ratios versus lead time for a rectangular region encompassing the southeast Maritime Continent and northeast Australia. The MJO predictability ratios are plotted for VP200 (Fig. 12a) and rainfall (Fig. 12b) considering all 120 MJO events combined from both the dynamical (thick solid blue) and persistence (thin dashed red) forecasts. The plots show that on average in this region the predictability ratio remains greater than 1 at lead times up until about 30 days for VP200 and 15 days for rainfall. In contrast the predictability ratio for the persistence forecasts remain greater than one only out to lead times of about 12 days for VP200 and 8 days for rainfall. This indicates a fair level of MJO forecast skill that might be attributed to the dynamical framework.

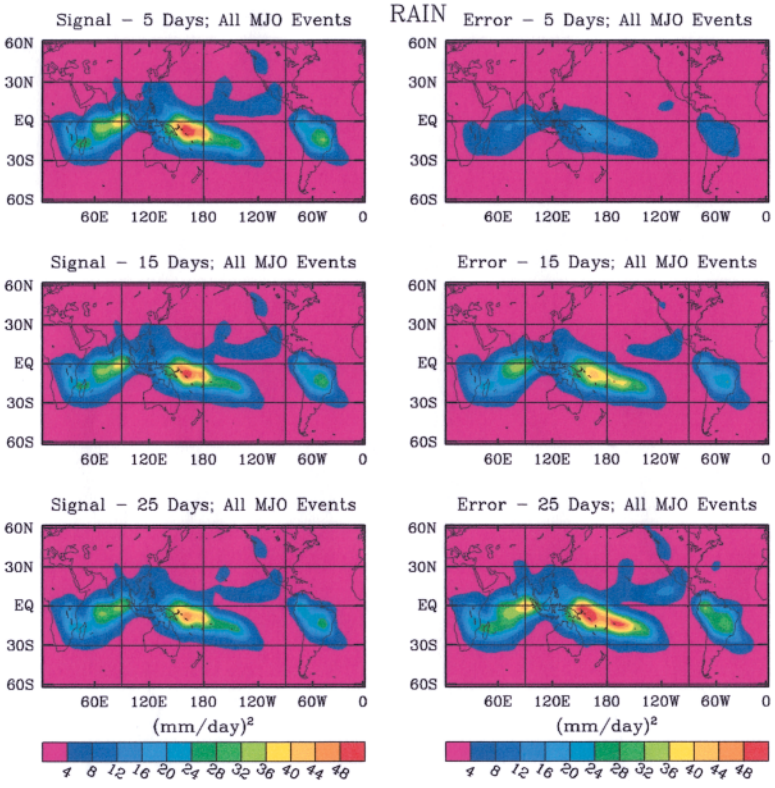

Fig. 11. Same as Fig. 10, except for rainfall.

The predictability values associated with the model's weather—that is, computed from unfiltered daily data—are also plotted in Figs. 12a,b for the same tropical region (thick solid black). For these cases, the predictability ratio remains greater than 1 only out to about 12 days for VP200 and 10 days for rainfall. Comparing these weather predictability ratios to the (dynamical) MJO predictability ratios discussed above

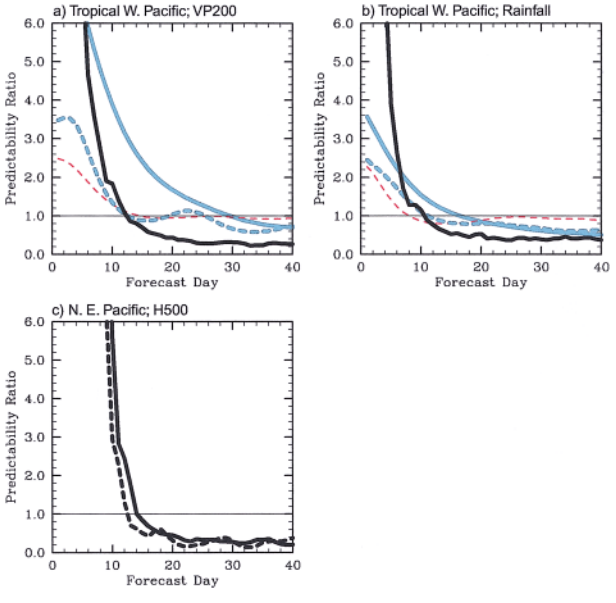

Fig. 12. Predictability ratios vs lead time [Eq. (5)] for (a) 200-hPa velocity potential (VP200) averaged over 8°N–16°S, 117.5°–167.5°E, (b) same as (a) except for rainfall, and (c) 500-hPa geopotential height averaged over 40°N–52°N, and 162.5°–142.5°W. Thick solid (thick dashed) lines are based on all 120 MJO (30 null) events from the dynamical forecasts. Thin dashed lines are based on all 120 MJO events from the persistence forecasts; see section titled "Summary" for computation of persistence. Blue and red (black) lines are based on calculations using daily filtered (unfiltered) data with *L* set equal to 25 (5) in Eq. (1), and thus are applicable to MJO (weather) variability.

illustrates the enhanced skill that is associated with predicting the low-frequency variations of the model's MJO over that of predicting its high-frequency weather variations. Figure 12c shows predictability ratios associated with the model's weather, in terms of H500, for a midlatitude regime (i.e., northeast Pacific Ocean). Again, it is clear that the limit of predictability for the model's weather, whether in the Tropics or the midlatitudes, is considerably shorter than the limit of predictability for the model's MJO. Finally, Figs. 12a–c all show the MJO predictability ratios computed from only the null events (thick dashed lines). Comparing the solid and dashed thick blue lines in Figs. 12a and 12b illustrate the enhanced predictability associated with strong MJO events versus the diminished predictability associated with periods when the MJO is weak/absent. Comparing the solid and dashed thick black lines in Fig. 12c illustrates that only modest sensitivity exists in the model's midlatitude weather predictability to the strength and/or presence of tropical MJO variability. Examination of the dependence of the model's midlatitude weather predictability to the phase of the MJO also showed very little sensitivity (not shown), with the exception that slightly greater predictability existed when the MJO convection center was located in the western Indian Ocean at the start of the forecast (i.e., phase 1+ in Figs. 4, 5). This latter issue is presently being examined in more detail and will be reported in a future study.

The results in Fig. 8 indicated the possibility that predictability of the model MJO may have some dependence on the convective versus subsidence phase of the MJO, as opposed the dependence on the longitudinal position of the convection (i.e., Fig. 5). To quantify the sensitivity of the predictability to the sign of the MJO anomaly (i.e., convection or subsidence), the relationship between the VP200 (rainfall) predictability ratios and the mean VP200 (rainfall) anomaly values were examined. Mean bandpassed VP200 and rainfall anomaly values over a given set of MJO events (i.e., Indian, Maritime, W Pacific and C Pacific phases) or null cases were computed as follows:

$$\overline{X_j^0} = \frac{1}{N}\sum_{i=1}^{N} X_{ij}^0 , \qquad (6)$$

where i represents the event index and N is 15. Note that this computation is tantamount to constructing the thick solid line shown in Fig. 7 for each grid point. These mean bandpassed anomalies [Eq. (6)] as well as the associated mean predictability ratios [Eq. (5)] each have latitude, longitude, forecast day, and MJO phase dependence. Both these variables were incorporated into the upper left (right) panels of Fig. 13 that show the VP200 (rainfall) predictability ratios bin averaged against the bandpassed VP200 (rainfall) anomaly and lead time from a large equatorial area that exhibits relatively strong intraseasonal variability. In this case, the latitude, longitude, and MJO phase (e.g., Fig. 5) dependencies were averaged out to leave only the dependence on lead time and mean anomaly value. These diagrams show that the predictability values, as defined in Eq. (5), tend to be slightly greater at longer lead times for the suppressed phase of the oscillation; this is especially so for rainfall. However at short lead times (< ~ 5 days), the model predictability for either variable tends to be greatest for the convective phase of the MJO. The lower panels of Fig. 13 indicate that the above tendencies, at least for rainfall (and VP200 at short lead times; not shown), are significant at the 95% level.

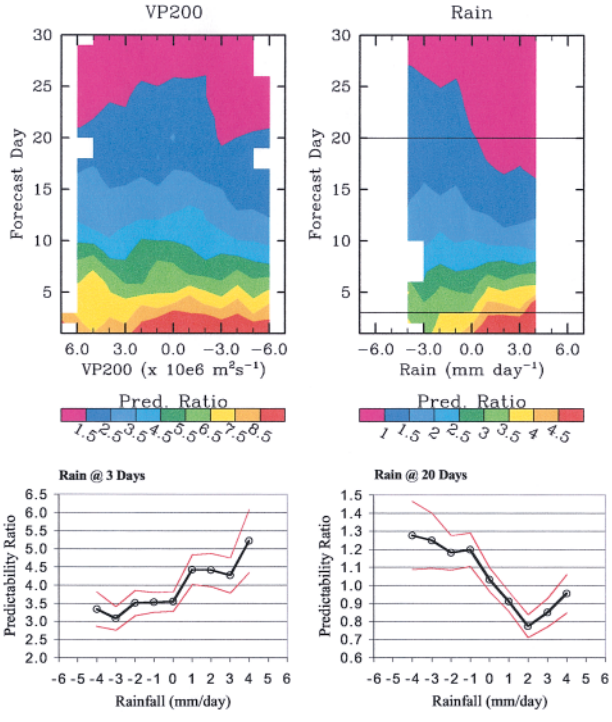

Fig. 13. (top) Mean predictability ratios [Eq. (5)] for (left) VP200 and (right) rainfall vs forecast day (vertical axis) and mean (left) VP200 and (right) rainfall anomaly value (horizontal axis). All four phases of the MJO were binned together with values taken from model grid points between 16°N–20°S and 20°E–130°W. Only bins with an *N* > 20 are plotted. (bottom) Thick lines are the predictability ratios of rainfall at forecast day (left) 3 and (right) 20 (see horizontal lines on upper-right plot). Thin lines are the 95% confidence intervals on the means using a Student's *t* test.

Finally, to examine the dependency of the predictability values discussed above on the modal characteristics of the model's intraseasonal variability and to demonstrate that the enhanced predictability at long lead times is in fact derived from the model's MJO, mean-square forecast errors were calculated for model EOF amplitude series. To do so, the filtered wintertime (November–April) bandpassed VP200 data from the control simulation were subject to a standard EOF analysis. The spatial structures of the first two EOF vectors resemble the middle two panels of the composite VP200 data shown in Fig. 5. Note that these first two EOF modes represent the basic structure of the model's MJO, particularly given that their time series have a maximum correlation (~ 0.8) at about ±12 days. EOF amplitude time series were computed using this modal structure for the control and perturbed forecasts for all the selected MJO events and null cases. These amplitude time series were then used in place of the actual data in Eqs. (1), (2), and (4) to compute the mean-square forecast error for each EOF mode. In this case, the forecasts for all four MJO phases and both perturbation sizes were considered together (N = 120).

The values of the mean-square forecast error for each EOF mode are shown in Fig. 14 versus forecast day. Also shown (asterisks,) are the variance percentages associated with the VP200 wintertime EOF modes. This figure demonstrates that the model forecast errors associated with the lowest two EOF modes, those that capture the main elements of the MJO, tend to be considerably lower at most lead times than the forecast errors for the higher order modes. In fact their forecast errors at lead times of 20–30 days are comparable to the forecast errors of the higher-order modes at 10–20 days. Keep in mind that given the significantly greater variance of the first two modes (~ 70% of the bandpassed variance), most of the overall error is still coming from these two modes. However, errors associated with the higher-order modes are likely to be influencing the development of errors of the lower-order modes. Note that for the null cases, the forecast errors for the low-order modes remain relatively small through the forecast period, even smaller than for the active MJO cases. This is somewhat expected since for these cases very little energy is associated with the low-order modes and thus the errors tend to remain small as well. In fact, the mean amplitudes [Eq. (3)] of EOF modes 1 and 2 (not shown) for the null cases are about 0.4 while those for the MJO events are about 1.0. These values, and their trends over the forecast period, are consistent with the lines associated with the MJO signal in the bottom two panels of Fig. 8. The implications of the above results will be discussed further below.

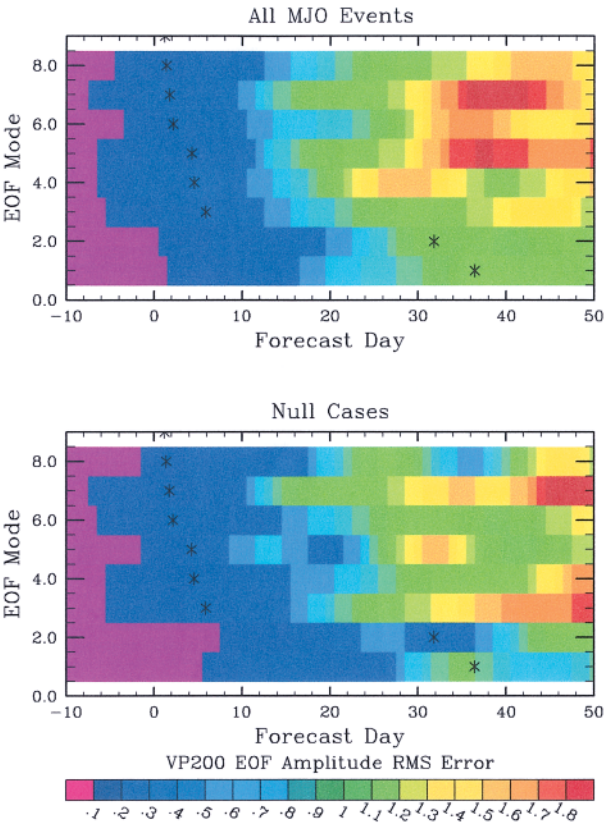

FIG. 14. Mean rms forecast errors [Eq. (4)] vs forecast day of the EOF time series (modes 1–8) of 200-hPa velocity potential for (top) all the selected MJO events combined and the (bottom) null cases. The asterisks indicate the percent variance associated with each EOF mode using the same *x* axis interpreted as percentage (%).

SUMMARY. The goal of this study is to provide an initial estimate of the dynamic predictability of the Madden–Julian oscillation (MJO). While there have been a number of predictive skill studies of the MJO (i.e., comparing forecasts to observations) with statistical forecast models as well as with dynamical models with rather poor representations of the MJO (see the introductory section), none of these provide a useful or adequate measure of dynamical MJO predictability. The NASA GLA general circulation model was chosen for this study due to its relatively realistic MJO representation (Fig. 2; see also Slingo et al. 1996; Sperber et al. 1996; Waliser et al. 2002, manuscript submitted to *Climate Dyn.*). A 10-yr control simulation using specified annual cycle SSTs was performed in order to provide initial conditions from which to

perform an ensemble of twin predictability experiments. The initial conditions were taken from periods of strong MJO activity identified via extended empirical orthogonal function (EOF) analysis of 30–90-day bandpassed tropical rainfall (Figs. 1, 3). From this analysis, 15 cases were chosen when the MJO convective center was located over the Indian Ocean, Maritime Continent, western Pacific Ocean, and central Pacific Ocean, respectively, making 60 cases in total (Figs. 3–5). In addition, 15 cases were selected that exhibited very little to no MJO activity (Figs. 3–5). Two different sets of small random perturbations were added to these 75 initial states. Simulations were then performed for 90 days from each of these 150 perturbed initial conditions (e.g., Fig. 7).

A measure of potential predictability was constructed based on a ratio of the signal associated with the MJO, in terms of rainfall or 200-hPa velocity potential (VP200), and the mean-square error between sets of twin forecasts [defined in Eqs. (1)–(5); see Figs. 6–8). Predictability was considered useful if this ratio was greater than 1, and thus if the mean-square error was less than the signal associated with the MJO. The results indicate that in the region of strong MJO variability (i.e., the Eastern Hemisphere), useful predictability for this model's MJO extends out to about 25–30 days for VP200 and to about 10–15 days for rainfall (Figs. 10–12). Note that these limits of predictability are associated with the relatively strong MJO event chosen for examination. During periods of little or no MJO activity, the limits of predictability over this same region are significantly diminished (e.g., Figs. 8, 12, and 14). Effectively, the same predictability ratios are found at considerably shorter lead times for the null cases versus the active MJO events (~ 5–15-day difference). This diminished predictability is a result of an error growth rate comparable to the strong MJO activity cases in combination with weaker intraseasonal signals. Thus, the magnitude of the error attains the size of the signal more rapidly within the forecast.

Predictability ratios were also computed for the model's weather variations (using unfiltered daily data), both for tropical and midlatitude regimes. For these cases, the predictability ratios remained above 1 only out to lead times of about 12 (10) days for tropical VP200 (rainfall) and 14 days for midlatitude 500-hPa geopotential height (Fig. 12). While this reduction in predictability for weather, relative to the MJO, is expected, the quantitative aspects of this result, along with its demonstration, emphasize the potential for enhancing our predictive capabilities of the atmosphere via the low-frequency variations of the MJO. In this regard, mean-square forecast errors were also computed for EOF amplitude time series of the bandpassed model output (Fig. 14) to highlight the fact that the enhanced predictability at the extended range is derived largely from the first two EOF modes, that is, the model's representation of the MJO.

The predictability measures for the MJO were also found to exhibit a modest dependence on the phase of the MJO, with greater predictability for the convective phase at short (< ~ 5 days) lead times and for the suppressed phase at longer (> ~ 15 days) lead times (Fig. 13). The reason for this dependence is not obvious. At short lead times, if the model atmosphere has built up sufficient vertical instability on a large scale, convection may be nearly ensured making the predictability higher. While in regions where convection is expected to be suppressed, the model may simply have a tendency toward convection making predictability at shorter lead times more difficult relative to convective regions. At longer lead times, pinpointing the place and time of convection may simply be more difficult than predicting what would typically be a larger-scale region of subsidence.

The above results have important implications for both the local regions that the MJO rainfall variations impact directly as well as regions that are influenced by the MJO via teleconnections. Present-day atmospheric forecasts are largely directed toward predicting short-term weather variations from analyzed initial conditions as well as seasonal climate variations associated with seasonal/interannual changes in surface boundary conditions, namely from tropical SSTs. As yet, operational weather forecasts have largely been unable to exploit the relatively strong signal and slow evolution associated with the MJO (e.g., Waliser et al. 1999a; Jones et al. 2000; Hendon et al. 2000). This is due to the generally poor representation of the MJO in most AGCMs, except for a few research-oriented models (e.g., Slingo et al. 1996; Waliser et al. 1999a; Waliser and Hogan 2000). However, if the MJO could be better represented in operational weather forecast models, the above results imply that extended-range tropical forecasts in the regions directly impacted by the MJO (e.g., Fig. 2) could be greatly enhanced and/or extended. This includes a means to better predict the onset and break periods of the Asian–Australian summer monsoons that are so strongly determined by intraseasonal variations such as the MJO. In this regard, the improvement in forecast skill that might be possible with a model capable of simulating the MJO over one that poorly represents the MJO can be inferred from the enhanced predictability associated with the active ver-

sus null MJO cases discussed above (i.e., about a 10-day improvement in lead time).

In addition to the local impacts that improved MJO prediction might offer there are a number of remote processes, discussed in the introductory section, whose prediction may also improve as well. These include wintertime midlatitude circulation anomalies, and their influence on U.S. west coast rainfall, as well as summertime precipitation variability over Mexico and South America. If the results above represent even an approximate estimate of the predictability of the observed MJO, then extended-range predictions (> 10 days) of this region's rainfall variability could be improved if our operational model representation's of the MJO were more realistic. In addition, recent studies have also shown that particular phases of the MJO are more favorable than others in regards to the development of tropical storms/hurricanes in both the Atlantic and Pacific sectors. Again having operational forecasts that provide useful skill in predicting the MJO out to even 10–15 days would be of benefit to predicting periods of enhanced or diminished periods of hurricane and tropical storm development.

There are a number of caveats that should be noted regarding the above results. For example, there are model shortcomings that suggest the above results might be an underestimate of predictability of the MJO. First, while the intraseasonal peak of equatorial wavenumber 1, upper-level velocity potential and zonal wind for the model is quite similar, in terms of magnitude and frequency, to observations, the model spectra has too much high-frequency (~days) variability for wavenumber 1 (Slingo et al. 1996). Relative to the MJO, this variability would be considered to be unorganized, errant convective activity that may erode the relatively smooth evolution of the MJO and thus diminish its predictability. Second, these simulations were carried out with fixed climatological SST values. A previous study with this model showed that coupled SSTs tend to have an enhancing and organizing influence on the MJO, making it stronger and more coherent (Waliser et al. 1999b). Thus the exclusion of SST coupling may lead to an underestimate of the predictability as well. The third aspect that may lead to an underestimate the predictability is the fact that the model contains too little variability over the western Indian Ocean and southern Maritime Continent region (Figs. 2, 12). The weakened MJO rainfall variations over this region may lead to a reduced predictability due to the model's relatively weak convection passing through this region, a region that exhibits a relatively robust convective signal in the observations. This tendency for underestimating the predictability is somewhat analogous to the manner the null cases showed reduced predictability, not because of an increased error growth rate but because of a reduced MJO signal.

A number of aspects associated with the model and/or analysis suggest that the above results might overestimate the predictability of the MJO. The first is that the model's coarse resolution and inherent reduced degrees of freedom relative to the true atmosphere may limit the amount of small-scale variability that would typically erode large time- and space-scale variability. However, it is important to note in this regard that the low-order EOFs of intrasesonality filtered model output typically do not capture as much variability as analogous EOFs of observed quantities (section titled "Experimental framework"). Thus while it may be true that the model lacks sufficient small-scale variability, which may erode MJO predictability, the model's MJO itself, as indicated above, still has room to be more robust and coherent, which would tend to enhance predictability. In addition to model shortcomings, the simple manner that perturbations were added to the initial conditions may also lead to an overestimate of the predictability. The perturbation structure and the size of the perturbations (see same section) may be too conservative and not adequately represent the type of initial condition error that would be found in an operational context. However, even if that is the case, it would seem that adequate size "initial" errors would occur in the forecast in a matter of a day or two and thus one would expect this aspect to overestimate the predictability by only a couple days, if at all. Future studies will examine the sensitivity of these results to the AGCM employed, to winter versus summer conditions, to SST coupling, midlatitude variability, and El Niño state, as well as to examine how sensitive these results are to the initial condition perturbations and definition of predictability [e.g., Eqs. (1)–(5)].

ACKNOWLEDGMENTS. Support for this study was provided by the National Science Foundation under Grants ATM-9712483 and ATM-0094416 (DW), and ATM-9712855 and ATM-009438 (CJ), and the National Oceanographic and Atmospheric Administration under Grant NA16GP2021. We would like to thank E. Kalnay, M. Ji, J. Roads, H. Van den Dool, S. Schubert and J. Anderson for their advice and comments. In addition, we would like to thank S. Nigam for his encouragement and foresight. This study's analysis and presentation benefited from the use of the NCAR Graphics Package and Seaspace Corporation's TeraScan software system.

REFERENCES

Anderson, J. L., and W. F. Stern, 1996: Evaluating the potential predictive utility of ensemble forecasts. *J. Climate,* **9,** 260–269.

Arakawa, A., and W. H. Schubert, 1974: Interaction of a cumulus cloud ensemble with the large-scale environment. Part I. *J. Atmos. Sci.,* **31,** 674–701.

——, and V. R. Lamb, 1977: Computational design of the basic dynamical processes of the UCLA general circulation model. *Methods in Computational Physics,* J. Chang, Ed., Vol. 17, Academic Press, 173–265.

Barnston, A. G., and Coauthors, 1994: Long-lead seasonal forecasts—Where do we stand? *Bull. Amer. Meteor. Soc.,* **75,** 2097–2114.

——, Y. He, and M. H. Glantz, 1999: Predictive skill of statistical and dynamical climate models in SST forecasts during the 1997–98 El Niño episode and the 1998 La Niña onset. *Bull. Amer. Meteor. Soc.,* **80,** 217–244.

Cane, M., and S. E. Zebiak, and S. C. Dolan, 1986: Experimental forecasts of El Niño. *Nature,* **321,** 827–832.

Charney, J., R. G. Fleagle, V. E. Lally, H. Riehl, and D. Q. Wark, 1966: The feasibility of a global observation and analysis experiment. *Bull. Amer. Meteor. Soc.,* **47,** 200–220.

Chen, T.-C., and J. C. Alpert, 1990: Systematic errors in the annual and intraseasonal variations of the planetary-scale divergent circulation in NMC medium-range forecasts. *Mon. Wea. Rev.,* **118,** 2607–2623.

Duchon, C. E., 1979: Lanczos filter in one and two dimensions. *J. Appl. Meteor.,* **18,** 1016–1022.

Ferranti, L., T. N. Palmer, F. Molteni, and K. Klinker, 1990: Tropical–extratropical interaction associated with the 30–60-day oscillation and its impact on medium and extended range prediction. *J. Atmos. Sci.,* **47,** 2177–2199.

Gates, W. L., and A. B. Nelson, 1975: A new (revised) tabulation of the Scripps topography on a one-degree global grid. Part 1: Terrain heights. Tech. Rep. R-1276-1-ARPA, The Rand Corporation, Santa Monica, CA, 132 pp.

Graham, N. E., and T. P. Barnett, 1995: ENSO and ENSO-related predictability. Part II: Northern Hemisphere 700-mb height predictions based on a hybrid coupled ENSO model. *J. Climate,* **8,** 544–549.

Harshvardhan, R. Davies, D. A. Randall, and T. G. Corsetti, 1987: A fast radiation parameterization for general circulation models. *J. Geophys. Res.,* **92,** 1009–1026.

Helfand, H. M., and J. C. Labraga, 1988: Design of a nonsingular level 2.5 second-order closure model for prediction of atmospheric turbulence. *J. Atmos. Sci.,* **45,** 113–132.

Hendon, H. H., and B. Liebmann, 1990a: A composite study of onset of the Australian summer monsoon. *J. Atmos. Sci.,* **47,** 2227–2240.

——, and ——, 1990b: The intraseasonal (30–50 day) oscillation of the Australian summer monsoon. *J. Atmos. Sci.,* **47,** 2909–2923.

——, ——, and J. D. Glick, 1998: Oceanic Kelvin waves and the Madden–Julian oscillation. *J. Atmos. Sci.,* **55,** 88–101.

——, ——, M. Newman, J. D. Glick, and J. Schemm, 2000: Medium range forecast errors associated with active episodes of the Madden–Julian oscillation. *Mon. Wea. Rev.,* **128,** 69–86.

Higgins, R. W., and S. D. Schubert, 1996: Simulations of persistent North Pacific circulation anomalies and interhemispheric teleconnections. *J. Atmos. Sci.,* **53,** 188–208.

——, and K. C. Mo, 1997: Persistent North Pacific circulation anomalies and the tropical intraseasonal oscillation. *J. Climate,* **10,** 224–244.

——, and W. Shi, 2001: Intercomparison of the principal modes of interannual and intraseasonal variability of the North American monsoon system. *J. Climate,* **14,** 403–417.

——, J. K. Schemm, W. Shi, and A. Leetmaa, 2000: Extreme precipitation events in the western United States related to tropical forcing. *J. Climate,* **13,** 793–820.

Jones, C., 2000: Occurrence of extreme precipitation events in California and relationships with the Madden–Julian oscillation. *J. Climate,* **13,** 3576–3587.

——, and J.-K. E. Schemm, 2000: The influence of intraseasonal variations on medium-range weather forecasts over South America. *Mon. Wea. Rev.,* **128,** 486–494.

——, D. E. Waliser, J. K. Schemm, and W. K. Lau, 2000: Prediction skill of the Madden–Julian oscillation in dynamical extended range forecasts. *Climate Dyn.,* **16,** 273–289.

Kalnay, E., R. Balgovind, W. Chao, D. Edelmann, J. Pfaendtner, L. Takacs, and K. Takano, 1983: Documentation of the GLAS fourth-order general circulation model. Vol. 1. NASA Tech. Memo. 86064, NASA Goddard Space Flight Center, Greenbelt, MD, 436 pp.

Kessler, W. S., and R. Kleeman, 2000: Rectification of the Madden–Julian oscillation into the ENSO cycle. *J. Climate,* **13,** 3560–3575.

——, M. J. McPhaden, and K. M. Weickmann, 1995: Forcing of the intraseasonal Kelvin waves in the equatorial Pacific. *J. Geophys. Res.,* **100,** 10 613–10 631.

Kirtman, B. P., J. Shukla, B. Huang, Z. Zhu, and E. K. Schneider, 1997: Multiseasonal predictions with a

coupled tropical ocean global atmosphere system. *Mon. Wea. Rev.,* **125,** 789–808.

Kleeman, R., and A. M. Moore, 1999: A new method for determining the reliability of dynamical ENSO predictions. *Mon. Wea. Rev.,* **127,** 694–705.

Lau, K. M., and P. H. Chan, 1986: Aspects of the 40–50-day oscillation during the northern summer as inferred from outgoing longwave radiation. *Mon. Wea. Rev.,* **114,** 1354–1367.

——, and T. J. Phillips, 1986: Coherent fluctuations of extratropical geopotential height and tropical convection in intraseasonal timescales. *J. Atmos. Sci.,* **43,** 1164–1181.

——, and P. H. Chan, 1988: Interannual and intraseasonal variations of tropical convection: A possible link between the 40–50-day oscillation and ENSO? *J. Atmos. Sci.,* **45,** 506–521.

——, and F. C. Chang, 1992: Tropical intraseasonal oscillation and its prediction by the NMC operational model. *J. Climate,* **5,** 1365–1378.

Liebmann, B., and D. L. Hartmann, 1984: An observational study of tropical–midlatitude interaction on intraseasonal timescales during winter. *J. Atmos. Sci.,* **41,** 3333–3350.

Lo, F., and H. H. Hendon, 2000: Empirical prediction of the Madden–Julian oscillation. *Mon. Wea. Rev.,* **128,** 2528–2543.

Lord, S. J., and A. Arakawa, 1980: Interaction of a cumulus cloud ensemble with the large-scale environment. Part 2. *J. Atmos. Sci.,* **37,** 2677–2962.

Lorenz, E. N., 1965: A study of the predictbility of a 28-variable atmospheric model. *Tellus,* **17,** 321–333.

——, 1982: Atmospheric predictability experiments with a large numerical model. *Tellus,* **34,** 505–513.

Madden, R. A., and P. R. Julian, 1971: Detection of a 40–50 day oscillation in the zonal wind in the tropical Pacific. *J. Atmos. Sci.,* **28,** 702–708.

——, and ——, 1972: Description of global-scale circulation cells in the Tropics with a 40–50-day period. *J. Atmos. Sci.,* **29,** 1109–1123.

——, and ——, 1994: Observation of the 40–50-day tropical oscillation—A review. *Mon. Wea. Rev.,* **122,** 814–837.

Maloney, E. D., and D. L. Hartmann, 2000: Modulation of eastern North Pacific hurricanes by the Madden–Julian oscillation. *J. Climate,* **13,** 1451–1460.

McPhaden, M. J., 1999: Climate oscillations—Genesis and evolution of the 1997–98 El Niño. *Science,* **283,** 950–954.

McPhaden, M. J., and B. A. Taft, 1988: Dynamics of seasonal and intraseasonal variability in the eastern equatorial Pacific. *J. Phys. Oceanogr.,* **18,** 1713–1732.

Mo, K. C., 2000: Intraseasonal modulation of summer precipitation over North America. *Mon. Wea. Rev.,* **128,** 1490–1505.

——, 2001: Adaptive filtering and prediction of intraseasonal oscillations. *Mon. Wea. Rev.,* **129,** 802–817.

——, and R. W. Higgins, 1998a: Tropical influences on California precipitation. *J. Climate,* **11,** 412–430.

——, and ——, 1998b: Tropical convection and precipitation regimes in the western United States. *J. Climate,* **11,** 2404–2423.

——, and ——, 1998c: The Pacific–South American modes and tropical convection during the Southern Hemisphere winter. *Mon. Wea. Rev.,* **126,** 1581–1596.

Nogués-Paegle, J., and K. C. Mo, 1997: Alternating wet and dry conditions over South America during summer. *Mon. Wea. Rev.,* **125,** 279–291.

Paegle, J. N., L. A. Byerle, and K. C. Mo, 2000: Intraseasonal modulation of South American summer precipitation. *Mon. Wea. Rev.,* **128,** 837–850.

Palmer, T. N., 1993: Extended-range atmospheric prediction and the Lorenz model. *Bull. Amer. Meteor. Soc.,* **74,** 49–66.

Phillips, T. J., 1996: Documentation of the AMIP models on the World Wide Web. *Bull. Amer. Meteor. Soc.,* **77,** 1191–1196.

Schneider, T., and S. M. Griffies, 1999: A conceptual framework for predictability studies. *J. Climate,* **12,** 3133–3155.

Sellers, P. J., Y. Mintz, Y. C. Sud, and A. Dalcher, 1986: A simple biosphere model (SiB) for use within general circulation models. *J. Atmos. Sci.,* **43,** 505–531.

Shapiro, R., 1970: Smoothing, filtering and boundary effects. *Rev. Geophys. Space Phys.,* **8,** 359–387.

Shukla, J., 1985: Predictability. *Advances in Geophysics,* Vol. 28B, Academic Press, 87–122.

Slingo, J. M., and Coauthors, 1996: Intraseasonal oscillations in 15 atmospheric general circulation models: Results from an AMIP diagnostic subproject. *Climate Dyn.,* **12,** 325–357.

Sperber, K. R., J. M. Slingo, P. M. Inness, and K.-M. Lau, 1996: On the maintenance and initiation of the intraseasonal oscillation in the NCEP/NCAR reanalysis and the GLA and UKMO AMIP simulations. *Climate Dyn.,* **13,** 769–795.

Stern, W., and K. Miyakoda, 1995: Feasibility of seasonal forecasts inferred from multiple GCM simulations. *J. Climate,* **8,** 1071–1085.

Sud, Y. C., and G. K. Walker, 1992: A review of recent research on improvement of physical parameterizations in the GLA GCM. *Physical Processes in Atmospheric Models,* D. R. Sikka and S. S. Singh, Eds., Wiley Eastern Ltd., 422–479.

Thompson, P. D., 1957: Uncertainty of initial state as a factor in the predictability of large scale atmospheric flow patterns. *Tellus,* **9,** 275–295.

Van den Dool, H. M., 1994: Long-range weather forecasts through numerical and empirical methods. *Dyn. Atmos. Oceans,* **20,** 247–270.

Waliser, D. E., and T. Hogan, 2000: Analysis of NOGAPS surface heat fluxes: Coupling to convection, cloud and dynamical processes. *J. Geophys. Res.,* **105,** 4587–4606.

——, C. Jones, J. K. Schemm, and N. E. Graham, 1999a: A statistical extended-range tropical forecast model based on the slow evolution of the Madden–Julian oscillation. *J. Climate,* **12,** 1918–1939.

——, K. M. Lau, and J.-H. Kim, 1999b: The influence of coupled sea surface temperatures on the Madden–Julian oscillation: A model perturbation experiment. *J. Atmos. Sci.,* **56,** 333–358.

——, Z. Zhang, K. M. Lau, and J.-H. Kim, 2001: Interannual sea surface temperature variability and the predictability of tropical intraseasonal variability. *J. Atmos. Sci.,* **58,** 2595–2614.

Wang, B., and H. Rui, 1990: Synoptic climatology of the transient tropical intraseasonal convection anomalies. *Meteor. Atmos. Phys.,* **44,** 43–61.

——, and X. Xie, 1997: A model for the boreal summer intraseasonal oscillation. *J. Atmos. Sci.,* **54,** 72–86.

Weickmann, K. M., 1983: Intraseasonal circulation and outgoing radiation modes during Northern Hemisphere winter. *Mon. Wea. Rev.,* **111,** 1838–1858.

——, 1991: El Niño/Southern Oscillation and Madden–Julian (30–60 day) oscillations during 1981–1982. *J. Geophys. Res.,* **96,** 3187–3195.

——, G. R. Lussky, and J. E. Kutzbach, 1985: Intraseasonal (30–60 day) fluctuations of outgoing longwave radiation and 250-mb streamfunction during northern winter. *Mon. Wea. Rev.,* **113,** 941–961.

Wheeler, M., and K. Weickmann, 2001: Real-time monitoring and prediction of modes of coherent synoptic to intraseasonal tropical variability. *Mon. Wea. Rev.,* **129,** 2677–2694.

Whitaker, J. S., and K. M. Weickmann, 2001: Subseasonal variations of tropical convection and week-2 prediction of wintertime western North American rainfall. *J. Climate,* **14,** 3279–3288.

Xie, P., and P. A. Arkin, 1997: Global precipitation: A 17-year monthly analysis based on gauge observations, satellite estimates, and numerical model outputs. *Bull. Amer. Meteor. Soc.,* **78,** 2539–2558.

Xue, Y.-K., P. J. Sellers, J. L. Kinter, and J. Shukla, 1991: A simplified biosphere model for global climate studies. *J. Climate,* **4,** 345–364.

Yang, X.-Q., J. L. Anderson, and W. F. Stern, 1998: Reproducible forced modes in the AGCM ensemble integrations and potential predictability of atmospheric seasonal variations in the extratropics. *J. Climate,* **11,** 2942–2959.

Yasunari, T., 1980: A quasi-stationary appearance of the 30–40 day period in the cloudiness fluctuations during the summer monsoon over India. *J. Meteor. Soc. Japan,* **59,** 336–354.